Fast-sum method for the elastic field of three-dimensional dislocation ensembles

Nasr M. Ghoniem and L. Z. Sun

Department of Mechanical and Aerospace Engineering, University of California, Los Angeles, California 90095-1597

(Received 20 January 1999)

The elastic field of complex shape ensembles of dislocation loops is developed as an essential ingredient in the dislocation dynamics method for computer simulation of mesoscopic plastic deformation. Dislocation ensembles are sorted into individual loops, which are then divided into segments represented as parametrized space curves. Numerical solutions are presented as fast numerical sums for relevant elastic field variables (i.e., displacement, strain, stress, force, self-energy, and interaction energy). Gaussian numerical quadratures are utilized to solve for field equations of linear elasticity in an infinite isotropic elastic medium. The accuracy of the method is verified by comparison of numerical results to analytical solutions for typical prismatic and slip dislocation loops. The method is shown to be highly accurate, computationally efficient, and numerically convergent as the number of segments and quadrature points are increased on each loop. Several examples of method applications to calculations of the elastic field of simple and complex loop geometries are given in infinite crystals. The effect of crystal surfaces on the redistribution of the elastic field is demonstrated by superposition of a finite-element *image force* field on the computed results. [S0163-1829(99)02625-9]

I. INTRODUCTION

Because the internal geometry of deforming crystals is very complex, a physically based description of plastic deformation can be very challenging. The topological complexity is manifest in the existence of dislocation structures within otherwise perfect atomic arrangements. Dislocation loops delineate regions where large atomic displacements are encountered. As a result, long-range elastic fields are set up in response to such large, localized atomic displacements. As the external load is maintained, the material deforms plastically by generating more dislocations. Thus, macroscopically observed plastic deformation is a consequence of dislocation generation and motion. A closer examination of atomic positions associated with dislocations shows that large displacements are confined only to a small region around the dislocation line (i.e., *the dislocation core*). The majority of the displacement field can be conveniently described as elastic deformation. Even though one utilizes the concept of dislocation distributions to account for large displacements close to dislocation lines, a physically based plasticity theory can paradoxically be based on the theory of elasticity.

The properties and interactions of simplified dislocation geometries have been the subject of intensive investigations for the past few decades.[1,2] The strength, mechanical, and some physical properties have been rationalized as a consequence of the dislocation behavior in materials. Methods for the evaluation of the elastic field of dislocations in materials are largely based on analytical solutions for special geometries of single dislocation lines, circular dislocation loops, or finite straight segments.[1,2] Interaction forces and energies between dislocations are also available in closed analytical forms for simplified dislocation line geometries, which involve series summations over Bessel functions[3] or elliptic integrals[4,-7].

Recently, a surge in interest in understanding the physical nature of plastic deformation has developed. This interest is motivated by extensive experimental evidence which shows that the distribution of plastic strain in materials is fundamentally heterogeneous.[8-10] Because of the complexity of dislocation arrangements in materials during plastic deformation, an approach which is based on direct numerical simulations for the motion and interactions between dislocations is now being vigorously pursued. One of the earliest attempts to study the interaction between dislocations and hardening obstacles by computer simulations is due to Forman.[11] In this method, a single dislocation loop was limited to move on glide planes between successive equilibrium configurations. However, the idea of computer simulation for the interaction between dislocation ensembles is a recent one. During the past decade, the approach of cellular automata was proposed by Lepinoux and Kubin[12] and that of dislocation dynamics by Ghoniem and Amodeo.[13,14] These early efforts were concerned with simplifying the problem by considering only ensembles of infinitely long, straight dislocations. The method was further expanded by a number of researchers,[15-24], showing the possibility of simulating reasonable, albeit simplified dislocation microstructure. To understand more realistic features of the microstructure in crystalline solids, Kubin, Canova, DeVincre, and co-workers[25-32] have pioneered the development of three-dimensional (3D) lattice dislocation dynamics. In this work, dislocation lines are discretized into linear straight segments which can occupy specified crystalline lattice sites. Dislocation line segments are limited to either screw or edge character for their Burgers vector. Recent advances made by Zbib, Hirth, and Rhee[33-35], and the work of Schwarz and co-workers[36-38] have contributed significantly to our understanding of complex dislocation reactions in crystalline 3D geometries. Straight line segments of arbitrary Burgers vector are considered in these developments.

The study of dislocation configurations at short range can be quite complex, because of large deformations and reconfiguration of dislocation lines during their interaction. Thus, adaptive gridding methods and more refined treatments of self-forces have been found to be necessary.[36-38] In some

special cases, however, simpler topological configurations are encountered. For example, long straight dislocation segments are experimentally observed in materials with high Peierel's potential barriers (e.g., covalent materials) or when large mobility differences between screw and edge components exist (e.g., some bcc crystals at low temperature). Under conditions conducive to glide of small prismatic loops on glide cylinders or the uniform expansion of nearly circular loops, changes in the loop *shape* are nearly minimal during its motion. Also, helical loops of nearly constant radius are sometimes observed in quenched or irradiated materials under the influence of point defect fluxes. It is clear that, depending on the particular application and physical situation one would be interested in a flexible method which can capture the essential physics at a reasonable computational cost. A consequence of the long-range nature of the dislocation elastic field is that the computational effort per time step is proportional to the square of the number of interacting segments. It is therefore advantageous to reduce the number of interacting segments within a given computer simulation or to develop more efficient approaches to computations of the long-range field.[14,24,34]

In this work, we aim at enhancing the current computational efforts on 3D dislocation dynamics (DD) (e.g., Ref. 25–38). We present here a numerical method for the determination of a key ingredient in DD computer simulations, that is, the elastic field of topologically complex dislocation ensembles. The main impetus for the present work is the need to describe the complex 3D topology of dislocation loops in the most flexible way. A wide spectrum of dislocation line deformations, ranging from highly curved to rigid body translations, arise within the same computational simulation. Existing methods are based on differential equations of motion for *straight* segments, where the elastic field variables affecting segment motion are computed at its center. When each segment moves under the influence of the stress field, the *connectivity* of the segments must be reestablished, resulting in a number of possible complications. The increase in the self-energy of the dislocation line has to be accounted for.[27] Additionally, when we consider forces on straight segments, we must necessarily deal with singular values of these forces at connectivity nodes[34]. Thus, problems of convergence as the segment length is decreased would naturally arise, because of the inherent numerical errors of computations. Computations of the self-force on a straight dislocation segment are also difficult, because of the need to describe local curvature, even though the segment is straight to begin with.[36] A modification of the Brown procedure[39] has been suggested to deal with this difficulty. Thus, the motivation behind the current work can be stated as follows:

(1) To reduce the computational burden by providing a high degree of flexibility in the selection of *both length and shape* of a dislocation segment.

(2) To avoid numerical problems arising from singularities at intersecting straight segments.

(3) To calculate the self-force on dislocation segments with a high degree of accuracy.

(4) To provide a flexible tool which sheds more light on the physics of close-range interactions involving in-plane high-curvature variations.
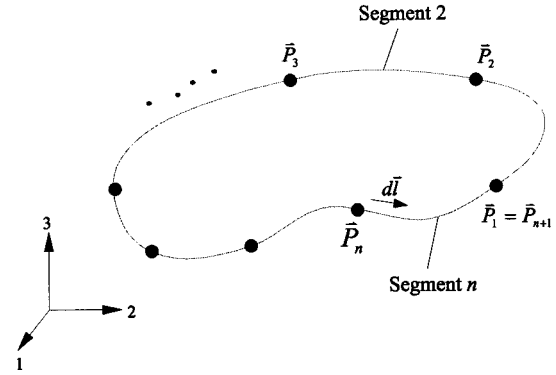
(5) To effectively deal with the physics of climb and

FIG. 1. A space dislocation loop discretized into a finite number of curved segments, N_s.

cross-slip, which require out-of-plane dislocation line curvature.

Although the theoretical foundations of dislocation theory are well-established (e.g., Refs. 1,2, and 40–42), efficient computational methods are still in a state of development (e.g., Refs. 30,34 and 43). Other than a few cases of perfect symmetry and special conditions,[3,4,6] the elastic field of 3D dislocations of arbitrary geometry is not analytically available. The field of dislocation ensembles is likewise analytically unattainable. We plan, therefore, to present the main elements of 3D dislocation theory such that the restrictions and limitations of the present computational method are clarified. The main steps in deriving equations for all field variables will thus be given, while the interested reader can find more helpful details in Refs. 7, 42, and 44. In Sec. II, we present the differential geometry of space dislocation loops, followed by a self-sufficient outline of the calculation procedure for the elastic field in Sec. III. Several test cases for verification of the proposed method are then given in Sec. IV. We compare calculation results for the stress field and energies of dislocation loops with those of known analytical and numerical solutions. Finally, conclusions from the work are discussed in Sec. V.

II. DIFFERENTIAL GEOMETRY OF DISLOCATION LOOPS

The core of an arbitrary-shape, 3D dislocation loop can be reduced to a continuous line. Assume that the dislocation line is segmented into (N_s) arbitrary curved segments, labeled $(1 \leq i \leq N_s)$., as shown in Fig. 1. For each segment, we define $\hat{\mathbf{r}}(u) = \mathbf{P}(u)$ as the position vector for any point on the segment, $\mathbf{T}(u) = T\mathbf{t}$ as the tangent vector to the dislocation line, and $\mathbf{N}(u) = N\mathbf{n}$ as the normal vector at any point (see Fig. 2). The space curve is then completely described by the parameter u, if one defines certain relationships which determine $\hat{\mathbf{r}}(u)$. Note that the position of any other point in the medium (Q) is denoted by its vector $\mathbf{r}$, and that the vector connecting the source point $\mathbf{P}$ to the field point is $\mathbf{R}$; thus $\mathbf{R} = \mathbf{r} - \hat{\mathbf{r}}$. In the following developments, we restrict the parameter $0 \leq u \leq 1$, although we map it later on the interval $-1 \leq \hat{u} \leq 1$ and $\hat{u} = 2u - 1$ in the numerical quadrature implementation of the method.

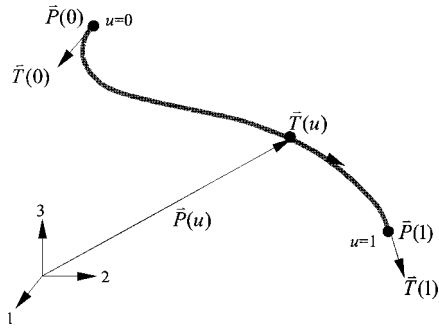To specify a parametric form for $\hat{\mathbf{r}}(u)$, we will now

FIG. 2. Basic elements of a space curve representing one dislocation segment.

choose a set of generalized coordinates $\mathbf{q}_i^{(j)}$ for each segment (j), which can be quite general. If one defines a set of basis functions $\mathcal{N}_i(u)$, where u is a parameter, and allows for index sums to extend also over the basis set $(i=1,2,\ldots,I)$, the equation of the segment can be written as

$$\hat{\mathbf{r}}^{(j)}(u)=\mathbf{q}_i^{(j)}\mathcal{N}_i(u). \tag{2.1}$$

Or in compact component (k) form, this can be put as

$$\hat{x}_k^{(j)}(u)=q_{ik}^{(j)}\mathcal{N}_i(u). \tag{2.2}$$

Thus, the components of the displacement vector are given by

$$\delta\hat{x}_k^{(j)}(u)=\delta q_{ik}^{(j)}\mathcal{N}_i(u). \tag{2.3}$$

At this point, we must specify the form of parametric description for the dislocation line. Although this step is open to pure computational convenience, we present here those parametric forms which we use later in this work. Parametric dislocation representations discussed below are also sufficient to describe the majority of experimentally observed dislocation line geometry.

A. Circular, elliptic, and helical loops

Small prismatic loops of circular (or nearly elliptic) shapes are observed in many materials under deformation, irradiation and quenching conditions.[45] Helical loops of unusual regularity have also been experimentally observed under large vacancy supersaturation.[45] Therfore, it seems natural to use a simple representation for such loops, where the shape functions are given by

$$\mathcal{N}_1=\cos(2\pi u), \qquad \mathcal{N}_2=\sin(2\pi u), \quad \mathcal{N}_3=u. \tag{2.4}$$

And their parametric derivatives, which we use later in determining the arc length, are simply given by

$$\mathcal{N}_{1,u}=-2\pi\mathcal{N}_2, \quad \mathcal{N}_{1,u}=2\pi\mathcal{N}_1, \quad \mathcal{N}_{3,u}=1. \tag{2.5}$$

Note that in this case the description is not in Cartesian coordinates and that the generalized degrees of freedom are given by

$$q_1=a, \quad q_2=b \quad \text{and} \quad q_3=c. \tag{2.6}$$

Loop motion is described in terms of the time variations of the generalized coordinates a,b, and c.

B. Linear parametric segments

The majority of 3D dislocation dynamics developments are based on analytic solutions to the elastic field of linear segments.[25–38]

Sometimes it is just as convenient to use a purely numerical method, without any loss of computational speed or accuracy.[43] Under these conditions, the *shape functions* $\mathcal{N}_i(u)$ and their derivatives $\mathcal{N}_{i,u}$ take the form

$$\mathcal{N}_1=1-u, \quad \mathcal{N}_2=u \tag{2.7}$$

and

$$\mathcal{N}_{1,u}=-1, \quad \mathcal{N}_{2,u}=1. \tag{2.8}$$

The available degrees of freedom for a *free* or *unconnected* linear segment (j) are just the position vectors of the beginning(j) and end $(j+1)$ nodes. Thus,

$$q_{1k}^{(j)}=P_k^{(j)}, \quad \text{and} \quad q_{2k}^{(j)}=P_k^{(j+1)}. \tag{2.9}$$

C. Cubic spline parametric segments

The self-force on a dislocation segment can be approximated as a simple function of its curvature.[1,2,46] To allow for continuity of the self-force along the entire dislocation loop and to capture nonlinear deformations of the dislocation line itself during, a higher-order parametric representation is desired. For cubic spline segments, we use the following set of shape functions, their parametric derivatives, and their associated degrees of freedom, respectively:

$$\mathcal{N}_1=2u^3-3u^2+1, \quad \mathcal{N}_2=-2u^3+3u^2,$$

$$\mathcal{N}_3=u^3-2u^2+u, \quad \text{and} \quad \mathcal{N}_4=u^3-u^2, \tag{2.10}$$

$$\mathcal{N}_{1,u}=6u^2-6u, \quad \mathcal{N}_{2,u}=-6u^2+6u2,$$

$$\mathcal{N}_{3,u}=3u^2-4u+1, \quad \text{and} \quad \mathcal{N}_{4,u}=3u^2-2u, \tag{2.11}$$

$$q_{1k}^{(j)}=P_k^{(j)}, \quad q_{2k}^{(j)}=P_k^{(j+1)}, \quad q_{3k}^{(j)}=T_k^{(j)},$$

$$\text{and} \quad q_{4k}^{(j)}=T_k^{(j+1)}. \tag{2.12}$$

D. Quintic spline parametric segments

A greater degree of flexibility can be achieved if one considers even higher-order representations. The special case of continuous quintic splines is rather interesting. The available degrees of freedom can be increased to include variations in the normal vector, $\mathbf{N}$, as well as the position $\mathbf{P}$ and tangent $\mathbf{T}$ vectors. So in passing from linear to cubic and then to quintic representations, one has $\{\mathbf{P}\}, \{\mathbf{P} \text{ and } \mathbf{T}\}$, and $\{\mathbf{P},\mathbf{T} \text{ and } \mathbf{N}\}$, respectively. With that, line curvature can be smoothly controlled and out-of-plane dislocation motion can be simultaneously followed with glide events. The equations for shape functions, their parametric derivatives, and available degrees of freedom for quintic splines are given by

$$\mathcal{N}_1=-6u^5+15u^4-10u^3+1, \quad \mathcal{N}_2=6u^5-15u^4$$

$$+10u^3, \quad \mathcal{N}_3=-3u^5+8u^4-6u^3+u, \tag{2.13}$$

$$\mathcal{N}_4 = -3u^5 + 7u^4 - 4u^3, \quad \mathcal{N}_5 = \frac{1}{2}(-u^5 + 3u^4 - 3u^3 + u^2),$$

and

$$\mathcal{N}_6 = \frac{1}{2}(u^5 - 2u^4 + u^3), \qquad (2.14)$$

$$\mathcal{N}_{1,u} = 30(-u^4 + 2u^3 - u^2), \quad \mathcal{N}_{2,u} = -\mathcal{N}_{1,u},$$

$$\mathcal{N}_{3,u} = -15u^4 + 32u^3 - 18u^2 + 1, \qquad (2.15)$$

$$\mathcal{N}_{4,u} = -15u^4 + 28u^3 - 12u^2,$$

$$\mathcal{N}_{5,u} = \frac{1}{2}(-5u^4 + 12u^3 - 9u^2 + 2u),$$

and

$$\mathcal{N}_{6,u} = \frac{1}{2}(5u^4 - 8u^3 + 3u^2), \qquad (2.16)$$

and

$$q_{1k}^{(j)} = P_k^{(j)}, \quad q_{2k}^{(j)} = P_k^{(j+1)}, \quad q_{3k}^{(j)} = T_k^{(j)},$$

$$q_{4k}^{(j)} = T_k^{(j+1)}, q_{5k}^{(j)} = N_k^{(j)},$$

and

$$q_{6k}^{(j)} = N_k^{(j+1)}. \qquad (2.17)$$

The total number of available degrees of freedom for a dislocation segment requires careful consideration. Even though more flexibility, and hence accuracy, is achieved by higher-order splines, it is still desirable to reduce the number of degrees (N_{DF}) of freedom from a computational standpoint. For a *free*, or *discrete* segment, N_{DF} is thus equal to the number of components in the Cartesian vector $\mathbf{q}_i^{(j)}$, i.e., $N_{DF} = 6$, 12, and 18, for linear, cubic, and quintic splines, respectively. However, N_{DF} can be greatly reduced on physical and geometric grounds. Since all segments must be connected on the loop, only one node is associated with each segment instead of two. Loop boundary conditions can be used to define (or fix) specific degrees of freedom (DF) on certain nodes. Thus, for a *continuous* representation, N_{DF} is reduced by a factor of 2. Moreover, if the motion is that of pure glide on the slip plane, appropriate coordinate transformations can be used to assign *local DF* in two dimensions. Thus, planar loop motion can be described by $N_{DF}^{local} = 2,4,6$ for the three parametric cases we consider here. Additional physical and geometric constraints can still be imposed to reduce N_{DF} even further.

Forces and energies of dislocation segments are given per unit length of the curved dislocation line. Also, line integrals of the elastic field variables are carried over differential line elements. Thus, if we express the Cartesian differential in the parametric form

$$dl_k^{(j)} = \hat{x}_{k,u}^{(j)} du = q_{sk}^{(j)} \mathcal{N}_{s,u} du, \qquad (2.18)$$

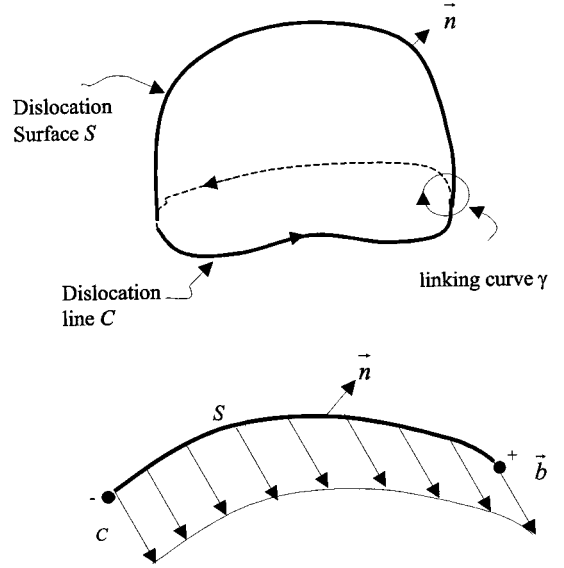the arc length differential for segment j is then given by

FIG. 3. Creation of a dislocation by a cut on the surface (S).

$$|dl^{(j)}| = (dl_k^{(j)} dl_k^{(j)})^{1/2} = (\hat{x}_{k,u}^{(j)} \hat{x}_{k,u}^{(j)})^{1/2} du \qquad (2.19)$$

$$= (q_{pk}^{(j)} \mathcal{N}_{p,u} q_{sk}^{(j)} \mathcal{N}_{s,u})^{1/2} du. \qquad (2.20)$$

III. ELASTIC FIELD VARIABLES AS FAST SUMS

As our main objective is to develop a computational method for numerical simulation of complex dislocation interactions, we need first to outline relevant theoretical foundations. In this section, we present a reasonably self-consistent discussion of isotropic elastic theory which leads to the present fast-sum computational implementation. A number of equivalent formulations are available in the literature.[2–47] However, because the present development is mainly computational, we follow the tensor index formulation of deWit,[7] Kröner,[4] and Kroupa.[6] For detailed derivations related to this section and its appendixes, the reader may consult Ref. 44.

A. Displacement field

The dislocation is formed by cutting over an arbitrary surface S, followed by *rigid* translation of the negative side of (S^-), while holding the positive side (S^+) fixed, as illustrated in Fig. 3. Define the dislocation line vector $\mathbf{t}$ as the tangent to the dislocation line. The Burgers vector $\mathbf{b}$ is prescribed as the displacement jump condition across the surface (S). The elastic field is based on the Burgers equation,[48] which defines the distribution of elastic displacements around dislocation loops. The strain tensor can be obtained from deformation gradients, while the stress tensor is readily accessible through linear constitutive relations. Once the stress and strain tensors are found, the elastic self-energy and interaction energy can be obtained. Referring to Fig. 3, we define the dislocation loop by cutting over the surface S and translating the negative side by the vector $\mathbf{b}$, while holding the positive side fixed. Along any *linking curve* γ, the closed line integral of the displacement vector is $\mathbf{b}$. Thus,

$$\mathbf{b}= \oint_\gamma d\mathbf{u} \quad \text{or} \quad b_i= \oint_\gamma u_{i,j}dx_j. \qquad (3.1)$$

For a given force distribution $f_m(\hat{\mathbf{r}})$ in the medium, the displacement vector is given by

$$u_k(\mathbf{r})= \int_{\text{all space}} U_{km}(\mathbf{r}-\hat{\mathbf{r}})f_m(\hat{\mathbf{r}})d^3\hat{\mathbf{r}}, \qquad (3.2)$$

where $U_{km}(\mathbf{r}-\hat{\mathbf{r}})$ are the isotropic elastic Green's functions, given by

$$U_{km}(\mathbf{R})= \frac{1}{8\pi\mu}\left[\delta_{km}R_{,pp} - \frac{\lambda+\mu}{\lambda+2\mu}R_{,km}\right],$$

where $R=\|\mathbf{R}\|$, μ and λ are Lamé constants. For the volume $\hat{V}$, bounded by the surface $\hat{S}$, and upon utilization of the divergence theorem for any rank tensor $\mathbf{T}:\int_{\hat{V}}\mathbf{T}_{,i}dV = \int_{\hat{S}}\mathbf{T}dS_i$, we obtain

$$u_m(\mathbf{r})= \int_{\hat{V}} U_{im}(\mathbf{r}-\hat{\mathbf{r}})f_i(\hat{\mathbf{r}})d\hat{V} - \int_S u_i(\hat{\mathbf{r}})C_{ijkl}U_{km,l}(\mathbf{r}-\hat{\mathbf{r}})d\hat{S}_j$$

$$+ \int_{\hat{S}} U_{im}(\mathbf{r}-\hat{\mathbf{r}})\sigma_{ij}(\hat{\mathbf{r}})d\hat{S}_j. \qquad (3.3)$$

The second and third terms in Eq. (3.3) account for displacement and traction boundary conditions on the surface $\hat{S}$, respectively. Assuming that body forces are absent in the medium, as well as any zero traction and rigid displacements b_i across the surface $\hat{S}$, we obtain

$$u_m(\mathbf{r})= -b_i \int_{\hat{S}} C_{ijkl}U_{km,l}(\mathbf{r}-\hat{\mathbf{r}})dS_j. \qquad (3.4)$$

For an elastic isotropic medium, the fourth-rank elastic constant tensor is given in terms of Lamé's constants μ and λ, and thus $C_{ijkl}=\lambda\delta_{ij}\delta_{kl}+\mu(\delta_{ik}\delta_{jl}+\delta_{il}\delta_{jk})$. Substituting in Eq. (3.4) and rearranging terms, the displacement vector is given by

$$u_m(\mathbf{r})= \frac{1}{8\pi} \int_{\hat{S}} b_m R_{,ppj}d\hat{S}_j$$

$$+ \frac{1}{8\pi} \int_{\hat{S}} (b_l R_{,ppl}d\hat{S}_m - b_j R_{,ppm}d\hat{S}_j)$$

$$+ \frac{1}{4\pi}\frac{\lambda+\mu}{\lambda+2\mu} \int_{\hat{S}} (b_j R_{,ppm}d\hat{S}_j - b_k R_{,kmj}d\hat{S}_j). \qquad (3.5)$$

Equation (3.5) can be converted to a line integral, if one recalls Stokes' theorem, extended to any rank tensor $\mathbf{T}$, expressed as: $\int_S \epsilon_{ijk}T_{abc\ldots,i}dS_k=\oint_C T_{abc}\ldots dl_j$. Noting the relationship between the Kronecker and permutation tensors, i.e., $\epsilon_{ijk}\epsilon_{klm}=\delta_{il}\delta_{jm}-\delta_{im}\delta_{jl}$, allows us to write Stokes' theorem as $\int_S (\delta_{il}\delta_{jm}-\delta_{im}\delta_{jl})T_{abc\ldots,j}dS_i = \oint_C \epsilon_{lmj}T_{abc}\ldots dl_j$. Using the substitution property of the Kronecker delta, Stokes' theorem can also be expressed in the coordinates with a caret in the following form:

$$\int_{\hat{S}}(T_{abc\ldots,m}d\hat{S}_l - T_{abc\ldots,l}d\hat{S}_m)= \oint_C \epsilon_{klm}T_{abc}\ldots dl_k. \qquad (3.6)$$

The first integral in Eq. (3.5) is the fraction of the solid angle Ω subtended by the loop times the Burgers vector (see Appendix A), while utilization of Eq. (3.6) can reduce the second and third terms to their line integral form. Therefore, a convenient form for the displacement vector components is given by

$$u_i= -\frac{b_i\Omega}{4\pi} + \frac{1}{8\pi} \oint_C \left[\epsilon_{ikl}b_l R_{,pp} + \frac{1}{1-\nu}\epsilon_{kmn}b_n R_{,mi}\right]dl_k. \qquad (3.7)$$

Equation (3.7) determines the displacement field of a single dislocation loop. For a loop ensemble, one can use the property of linear superposition. Thus, the line integral in Eq. (3.7) can be converted into a fast numerical sum over the following set: quadrature points ($1\le\alpha\le Q_{\max}$) associated with weighting factors (w_α), loop segments ($1\le\beta\le N_s$), and number of ensemble loops ($1\le\gamma\le N_{\text{loop}}$). Therefore, a computational form for the displacement vector is

$$u_i= \frac{1}{4\pi} \sum_{\gamma=1}^{N_{\text{loop}}} \left\{ -b_i\Omega + \frac{1}{2} \sum_{\beta=1}^{N_s} \sum_{\alpha=1}^{Q_{\max}} w_\alpha \right.$$

$$\left. \times \left(\epsilon_{ikl}b_l R_{,pp} + \frac{\epsilon_{kmn}b_n R_{,mij}}{1-\nu}\right)\hat{x}_{k,u}\right\}. \qquad (3.8)$$

In Appendix A, we list successive derivatives for the modulus of the radius vector $\mathbf{R}$, surface and line integral forms of the solid angle Ω, and its derivatives. Detailed derivation steps in the equation sequence can be reviewed in Ref. 44.

B. Strain and stress fields

Once the displacement field is determined, the strain and stress fields can be readily obtained. If we denote the deformation gradient tensor by $u_{i,j}$, the strain tensor e_{ij} in infinitesimal elasticity is its symmetric decomposition: $u_{i,j} = \frac{1}{2}(u_{i,j}+u_{j,i})+\frac{1}{2}(u_{i,j}-u_{j,i})=e_{ij}+\omega_{ij}$, where ω_{ij} is the rotation tensor. Taking the derivatives of Eq. (3.7) yields the deformation gradient tensor

$$u_{i,j}= -\frac{b_j\Omega_{,i}}{4\pi}$$

$$+ \frac{1}{8\pi} \oint_C \left[\epsilon_{jkl}b_l R_{,ppi} + \frac{1}{1-\nu}\epsilon_{kmn}b_n R_{,mij}\right]dl_k, \qquad (3.9)$$

from which the following strain tensor is obtained:

$$e_{ij} = -\frac{b_i\Omega_{,j} + b_j\Omega_{,i}}{8\pi}$$

$$+ \frac{1}{8\pi} \oint_C \left[\frac{1}{2}(\epsilon_{jkl}b_lR_{,i} + \epsilon_{ikl}b_lR_{,j})_{,pp} \right.$$

$$\left. + \frac{\epsilon_{kmn}b_nR_{,mij}}{1-\nu} \right] dl_k . \tag{3.10}$$

The derivatives of the solid angle Ω are given by Eq. (A2) in Appendix A, which can now be used to derive the strain tensor components as line integrals:

$$e_{ij} = \frac{1}{8\pi} \oint_C \left[-\frac{1}{2}(\epsilon_{jkl}b_iR_{,l} + \epsilon_{ikl}b_jR_{,l} \right.$$

$$\left. - \epsilon_{ikl}b_lR_{,j} - \epsilon_{jkl}b_lR_{,i})_{,pp} + \frac{\epsilon_{kmn}b_nR_{,mij}}{1-\nu} \right] dl_k . \tag{3.11}$$

Similar to Eq. (3.8), the fast-sum equivalent of Eq (3.11) is now given by

$$e_{ij} = \frac{1}{8\pi} \sum_{\gamma=1}^{N_{\text{loop}}} \sum_{\beta=1}^{N_s} \sum_{\alpha=1}^{Q_{\text{max}}} w_\alpha \left(-\frac{1}{2}(\epsilon_{jkl}b_iR_{,l} + \epsilon_{ikl}b_jR_{,l} \right.$$

$$\left. - \epsilon_{ikl}b_lR_{,j} - \epsilon_{jkl}b_lR_{,i})_{,pp} + \frac{\epsilon_{kmn}b_nR_{,mij}}{1-\nu} \right) \hat{x}_{k,u} . \tag{3.12}$$

To deduce the stress tensor, we use the isotropic stress-strain relations of linear elasticity. First, the dilatation is obtained by letting $i = j = r$ in Eq. (3.11) above:

$$e_{rr} = -\frac{1}{8\pi}\frac{1-2\nu}{1-\nu} \oint_C \epsilon_{kmn}b_nR_{,mrr}dl_k . $$

Using the stress-strain relations $\sigma_{ij} = 2\mu e_{ij} + \lambda e_{rr}\delta_{ij}$, we can readily obtain the stress tensor

$$\sigma_{ij} = \frac{\mu b_n}{4\pi} \oint_C \left[\frac{1}{2}R_{,mpp}(\epsilon_{jmn}dl_i + \epsilon_{imn}dl_j) + \frac{1}{1-\nu}\epsilon_{kmn}(R_{,ijm} \right.$$

$$\left. - \delta_{ij}R_{,ppm})dl_k \right] . \tag{3.13}$$

The *computational* fast sum for the stress tensor is given below in compact form, while explicit representations are listed in Appendix B:

$$\sigma_{ij} = \frac{\mu}{4\pi} \sum_{\gamma=1}^{N_{\text{loop}}} \sum_{\beta=1}^{N_s} \sum_{\alpha=1}^{Q_{\text{max}}} b_n w_\alpha \left[\frac{1}{2}R_{,mpp}(\epsilon_{jmn}\hat{x}_{i,u} + \epsilon_{imn}\hat{x}_{j,u}) \right.$$

$$\left. + \frac{1}{1-\nu}\epsilon_{kmn}(R_{,ijm} - \delta_{ij}R_{,ppm})\hat{x}_{k,u} \right] . \tag{3.14}$$

C. Interaction energy and self-energy

The mutual interaction between two dislocation loops can be obtained by a volume integration of the energy density resulting from the stress field of one loop, acting on the strain field of the other, as given below:

$$E_I = \int_V \sigma_{ij}^{(1)}e_{ij}^{(2)}dV, \tag{3.15}$$

where $\sigma_{ij}^{(1)}$ is the elastic stress field from the first dislocation loop and $e_{ij}^{(2)}$ is the elastic strain tensor originating from the second one. After a lengthy derivation, deWit[7] provided a simple double line integral formulation for the interaction energy as

$$E_I = -\frac{\mu b_i^{(1)}b_j^{(2)}}{8\pi} \oint_{C^{(1)}} \oint_{C^{(2)}} \left[R_{,kk}\left(dl_j^{(2)}dl_i^{(1)} \right. \right.$$

$$\left. \left. + \frac{2\nu}{1-\nu}dl_i^{(2)}dl_j^{(1)} \right) + \frac{2}{1-\nu}(R_{,ij} - \delta_{ij}R_{,ll})dl_k^{(2)}dl_k^{(1)} \right] . \tag{3.16}$$

In Eq. (3.16), the line integral is carried over the two space curves $C^{(1)}$ and $C^{(2)}$. Thus, the corresponding fast sum for the interaction energy reads

$$E_I = -\frac{\mu b_i^{(1)}b_j^{(2)}}{8\pi} \sum_{\beta^{(1)}=1}^{N_s^{(1)}} \sum_{\beta^{(2)}=1}^{N_s^{(2)}} \sum_{\alpha^{(1)}=1}^{Q_{\text{max}}^{(1)}} \sum_{\alpha^{(2)}=1}^{Q_{\text{max}}^{(2)}} w_{\alpha^{(1)}}w_{\alpha^{(2)}}$$

$$\times \left[R_{,kk}\left(\hat{x}_{j,u}^{(2)}\hat{x}_{i,u}^{(1)} + \frac{2\nu}{1-\nu}\hat{x}_{i,u}^{(2)}\hat{x}_{j,u}^{(1)} \right) \right.$$

$$\left. + \frac{2}{1-\nu}(R_{,ij} - \delta_{ij}R_{,ll})\hat{x}_{k,u}^{(2)}\hat{x}_{k,u}^{(1)} \right] . \tag{3.17}$$

The self-energy of a single dislocation loop can be calculated as half the interaction energy between two identical dislocation loops separated by a distance r_0. The contribution to the self-energy from the dislocation core can be estimated from atomistic calculations, and is usually on the order of 5–10 % of the self-energy.[6] However, the core contribution can be incorporated by adjusting the value of r_0. In a fairly rough evaluation, we may take the core energy into account by setting $r_0 = b/2$. (cf. Ref. 7).

IV. RESULTS AND METHOD VALIDATION

In this section, we discuss several test cases which both illustrate the utility of the fast-sum method and validate its accuracy. We will first present results of computations for the elastic field of isolated circular shear and prismatic dislocation loops. Since some analytical solutions are available for these cases, we will compare the results of the fast-sum method to analytical results. The issues of numerical convergence and accuracy are also discussed. In the latter part of this section, we present results of calculations of the elastic field of typical complex-shape loops, representing familiar Frank-Read dislocation sources in crystalline materials.

A. Stress field of simple loops

1. Circular slip loop

We consider here the stress distribution in the vicinity of a shear (slip) loop in a bcc crystal. The circular loop has a
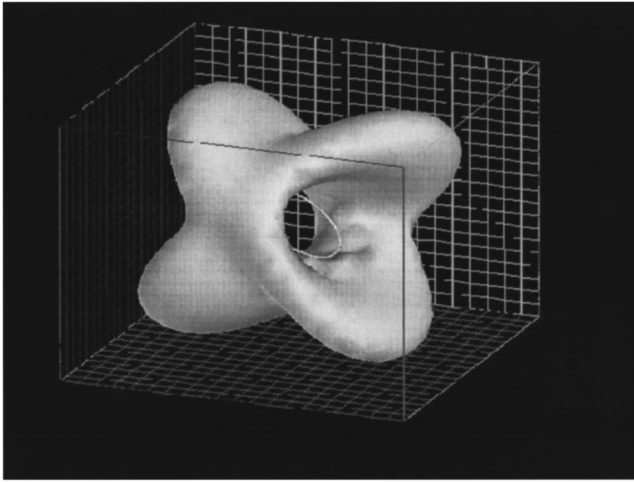
FIG. 4. Normal stress isosurface σ_{11} in the local loop coordinates, where the one-axis is the [010] direction and the three-axis is the [110]direction.

radius of $200|\mathbf{b}|$. The loop is oriented for primary slip [i.e., $(110)/\frac{1}{2}\{111\}$]. In the figures shown in this section, all distances are given in units of $|\mathbf{b}|$, while stress values are relative to μ. In the local coordinates of the (110) plane, Figure 4 shows an isosurface for the normal stress around the dislocation loop. It is clear that the stress surface has an orientational dependence on the $\langle 111 \rangle$-slip direction. On the glide plane itself, the normal stress vanishes, while the stress surface is symmetric with respect to the loop center. The shear stress components σ_{12} and σ_{23} are displayed in Figs. 5 and 6. While σ_{12} shows a characteristic ''lope'' structure of the isosurface, σ_{23} displays a crescent shape. The maximum width of the crescent is for pure edge, while the stress vanishes for the screw component of the loop.

The convergence and computational speeds of the fast-sum method are demonstrated in Ref. 43. The dependence of the numerical results on the number of segments, segment spline type, and quadrature indicates that the method is numerically convergent, as the number of segments and/or
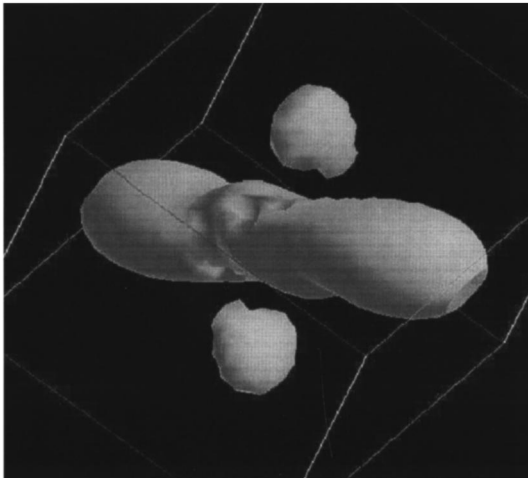

FIG. 5. Shear stress isosurface σ_{12} in the local loop coordinates, where the one-axis is the [010] direction and the three-axis is the [110] direction.
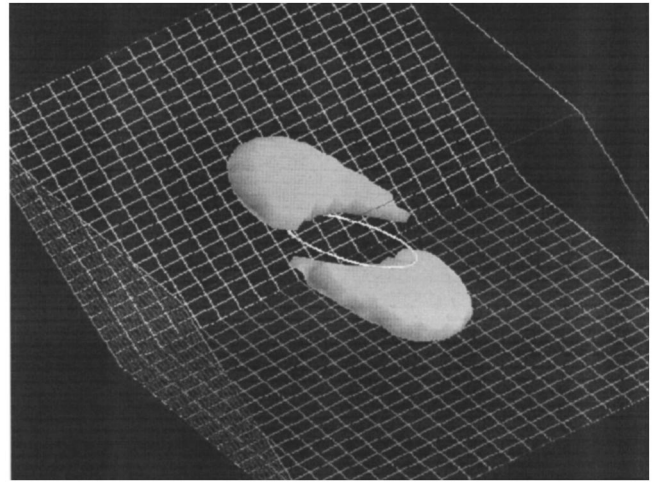

FIG. 6. Shear stress isosurface σ_{23} in the local loop coordinates, where the one-axis is the [010] direction and the three-axis is the [110] direction.

quadrature integration points is increased.[43] The issue of the numerical accuracy of the method is addressed next, by comparison to one of the few available analytical solutions in the literature.

2. Circular prismatic loop

Kroupa[5,6] derived analytical solution for the stress field of a prismatic circular dislocation loop in an infinite isotropic medium. His explicit out-of-plane normal stress in the loop plane (i.e., $z=0$) σ_{zz} reads

$$\frac{\sigma_{zz}}{\mu b/2\pi R(1-\nu)} = \frac{2}{1-(x/R)^2} E\left(\frac{x}{R}\right) \qquad \left(0 \leq \frac{x}{R} < 1\right),$$
(4.1)

$$\frac{\sigma_{zz}}{\mu b/2\pi R(1-\nu)} = 2\frac{R}{x}\left[K\left(\frac{R}{x}\right) - \frac{1}{1-(R/x)^2} E\left(\frac{R}{x}\right) \right]$$

$$\left(\frac{x}{R} > 1\right), \quad (4.2)$$

where K and E are the complete elliptic integrals of the first and second kinds, respectively, x is the distance from loop center, and R is the loop radius.

In order to evaluate the accuracy of the present fast-sum method, a comparison between Kroupa's analytical solution for the normal stress component σ_{zz} of a circular prismatic loop and our numerical calculations is shown in Fig. 7. It can be seen that the error in the value of the normal stress depends on the number of segments and on the distance between the field point and the dislocation core. The normal stress shows the characteristic asymmetric singularity at the dislocation line, where the stress field decays to zero at large distances from the core, while it remains finite at the loop center. A more quantitative measure of the error is shown in Fig. 8, where the percent error between the numerical and analytical solutions is shown as a function of distance along the x axis on the loop plane. It is seen that the numerical accuracy is below 4% for only four cubic spline segments,
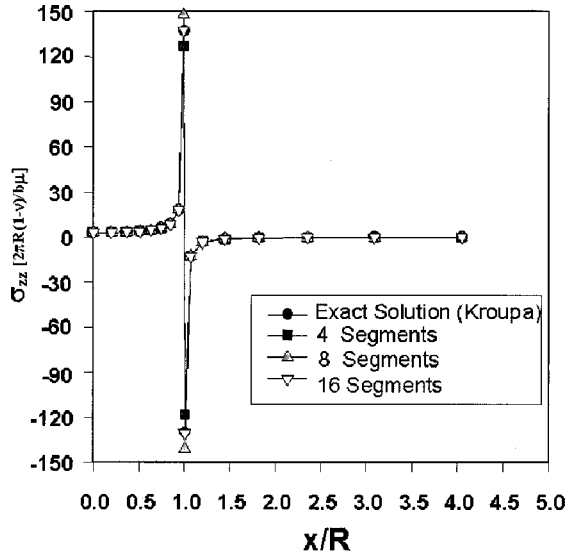
FIG. 7. A comparison between numerical (current method) and exact analytical (Kroupa) solutions for the normal stress component σ_{zz} of a circular prismatic loop.

except very close to the dislocation core. The number of quadrature integration points is kept at 16 for all cases studied in the figure. The highest error (below 9%) is manifest at distances less than $1.5|\mathbf{b}|$ from the dislocation core, when the number of segments is less than 8. However, the maximum error is less than 0.3% at such close distances, when the number of segments is increased to 16. It is important to note that such high accuracy is needed in calculations of the self-force via the Brown formula[39] or its variants.[46,37] When the stress field is averaged at distances of $\pm \epsilon$ from the dislocation core, the singularity is removed and a convergent, finite self-force is obtained. Thus, the accuracy of field evaluation is apparent.

B. Interaction energy and self-energy

To demonstrate the capability of our fast-sum calculation of the interaction energy (E_I), we specify the two dislocations to be pure prismatic coaxial circular loops of equal
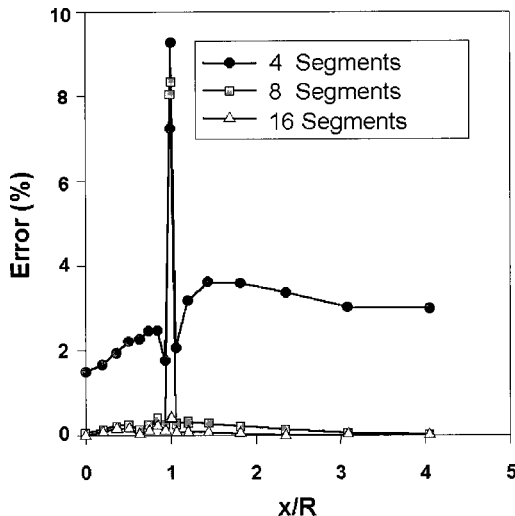
FIG. 8. Dependence of the error between numerical and analytical (Kroupa) normal stress results on the distance from loop center, for various number of segments.
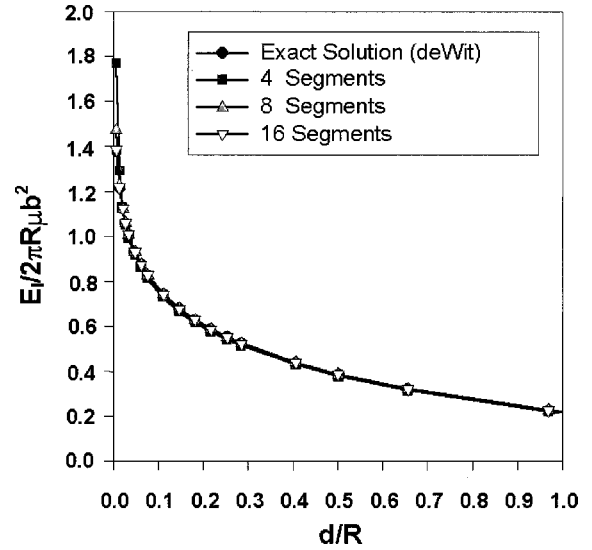

FIG. 9. A comparison between numerical (current method) and analytical (deWit) results for the interaction energy between two prismatic loops.

radius and of the same Burgers vector. In such a case, the exact analytical result is available from Ref. 7 as

$$\frac{E_I}{2\pi R \mu b^2} = \frac{\kappa}{2\pi(1-\nu)}[K(\kappa) - E(\kappa)], \qquad (4.3)$$

in which $\kappa = 1/[1+(d/2R)^2]^{1/2}$ and d is the normal distance between the two parallel loop planes. Figure 9 shows the results of our calculations, as compared with exact analytical results. The interaction energy is shown as a function of distance between the two loop planes. While the number of quadrature integration points in these calculations is kept at 128, the interaction energy is convergent as the number of segments is increased. This is particularly important at close distances, as can be seen from the figure.

Furthermore, Hirth and Lothe[2] provided an explicit expression for the self-energy of a circular slip loop as

$$\frac{E_s}{2\pi R \mu b^2} = \frac{2-\nu}{8\pi(1-\nu)}\left[-\ln\left(\tan\frac{\rho}{4R}\right) - 2\cos\frac{\rho}{2R}\right],$$
$$(4.4)$$

where ρ is the dislocation core size and is taken as $1/2|\mathbf{b}|$, as suggested by deWit.[7] Figure 10 shows the dependence of the self-energy on the loop radius, computed numerically, and compared to the analytical solutions.[2] The percent error between the numerical and analytical results is shown in Fig 11. It is interesting to note that, even for four cubic spline segments, the error is rather small (a few percent), when the loop radius is in the tens to hundreds of $|\mathbf{b}|$. However, it is clearly demonstrated that more spline segments are necessary for larger size loops, and that the error can generally be brought down below 1%.

C. Complex loop geometries

1. Single Frank-Read source

In typical dislocation dynamics computer simulations, heavy initial dislocation microstructure is introduced, and its
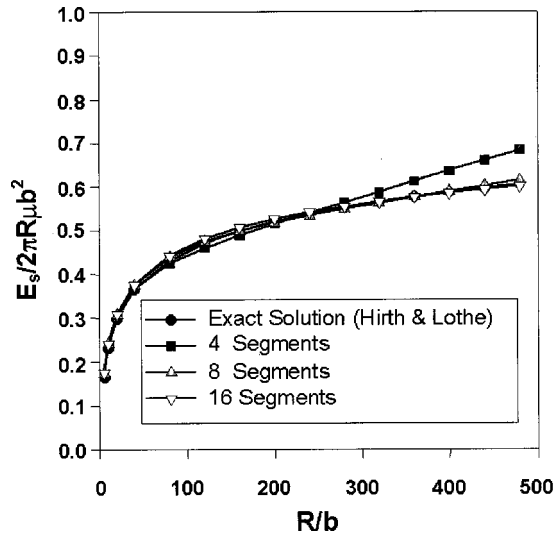
FIG. 10. A comparison between numerical (current method) and analytical (Hirth-Lothe) results for the self-energy of a slip loop.

subsequent evolution is followed by solving appropriate equations of motion. Visualization of the stress field associated with the evolving microstructure requires additional techniques to mask specific features; otherwise the 3D computer image is hopelessly complicated to be useful. Nonetheless, it is instructive to investigate the nature of the elastic field resulting from reasonably complex loop configurations. In this section, we present results for two common dislocation problems: an isolated Frank-Read (FR) dislocation loop and two interacting such sources in a molybdenum single crystal. An initial straight edge dislocation segment, lying on the $(1\bar{1}1)$ plane, is subjected to an applied stress. The pinned ends of the segment are located at $x = \pm 100|\mathbf{b}|$ from the plane center of the crystal. The expansion of the dislocation segment results in the dislocation loop, shown in Fig. 12, before annihilation of the two opposite screw components takes place. The pinned ends of the source are connected to
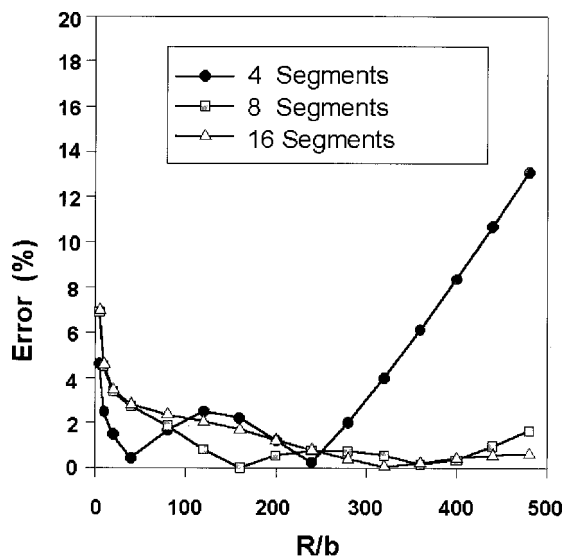

FIG. 11. Dependence of the error between numerical and analytical solutions in Fig 10 above on the loop radius and number of cubic spline segments.
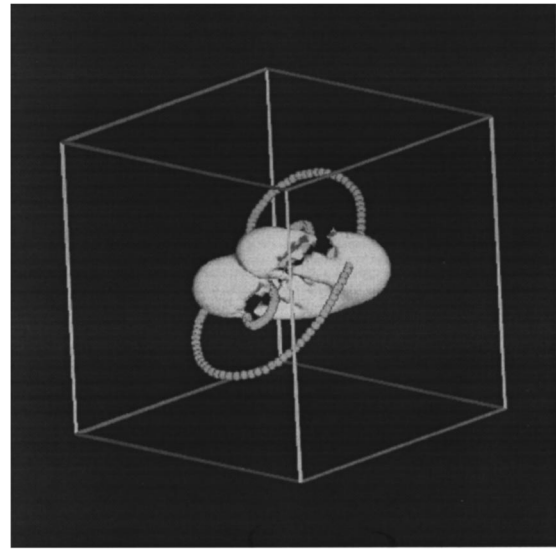

FIG. 12. Normal stress isosurface (186 MPa) σ_{11} for a single Frank-Read source in molybdenum.

the crystal surface by two rigid threading dislocations. Figure 12 shows the normal stress isosurface of 186 MPa associated with the FR loop. The isosurface shows orientational dependence on the Burgers vector, as well as symmetry with respect to the (111) plane. Note the ''dimples'' in the stress surface which result from the deviation of the FR loop from perfect circular symmetry, as investigated in the earlier section.

So far, we have assumed that the crystal is elastically isotropic and of infinite dimensions. The solution method relies on the existence of analytic forms for the elastic Green's functions, and those are not available for finite media. Recently, Cleveringa, Van der Giessen, and Needleman[49] have proposed a superposition method to satisfy the boundary conditions of crystals under external constraints. First, the surface traction resulting from the interaction of the dislocation loop with the crystal surface is computed. Once this is achieved, a finite-element method (FEM) is used to calculate the stress field resulting from the same traction, with a reversed sign (so-called image traction) in addition to other externally applied forces. The case of a free crystal is somewhat special, because only image traction boundary conditions can be imposed at the surface. Thus, since a full dislocation loop is mechanically balanced, only rigid body displacements need to be carefully eliminated. We choose here to use the threading dislocation arms, which intersect the surface at two points, to eliminate rigid body rotation and translation. To show the effects of crystal boundaries, we follow the FEM approach, as suggested by Cleveringa et al.[49] Figure 13 shows the results of FEM calculations for the normal stress component on the crystal surface, resulting from image traction. It is clear that the FR source is pulling on the upper surface and that additional stress concentrations on the x-z surface are associated with the rigid arms of the threading dislocation. The image shear stress σ_{13} is also shown in Fig. 14, where the surface displacements of the crystal are scaled to show the shape of a free crystal which contains a FR source. Note the symmetry with respect to the (111) plane of positive and negative
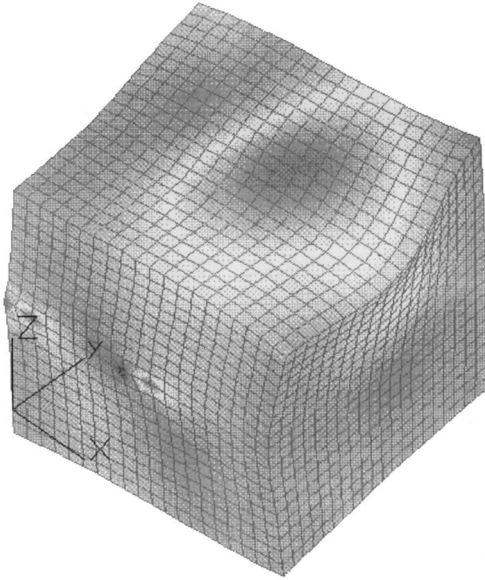
FIG. 13. Normal stress distribution resulting from the interaction of the single FR source with the surface of a molybdenum single crystal.

shear, and the high shear stress around the end points of the threading dislocation.

2. Interacting FR dislocation loops

When FR sources are activated on the same or neighboring slip planes, very complex patterns can emerge.[37] Interaction of FR sources appears to be one of the main mechanisms which control complex dislocation patterns. For this reason, we study the stress field of two such FR sources, which are both located on the $(1\bar{1}1)$ plane. The length of each initial straight edge segment is taken as $150|\mathbf{b}|$. One pinned end of the first FR source is located at $x=225|\mathbf{b}|$ and at $x=-225|\mathbf{b}|$ for the second source. The other end is located by
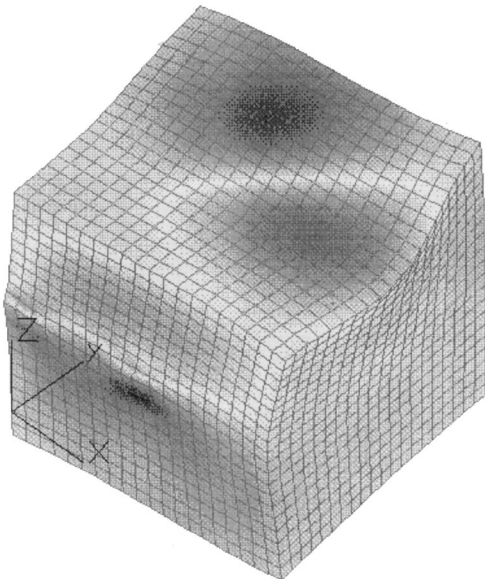

FIG. 15. Normal stress isosurface (-130 MPa), σ_{33}, for two interacting Frank-Read sources in molybdenum.

rotating the initial segment (i.e., length$=150|\mathbf{b}|$ with an angle of $\theta=220°$ and $\theta=100°$ for the first and second FR sources, respectively.

The normal stress $\sigma_{33}=-130$ MPa is shown in Fig 15, while the stress isosurface $\sigma_{11}=-2000$ MPa is shown in Fig. 16. The stress σ_{33} isosurface shows a split about the (111) plane, but because of the initial lack of symmetry of the dislocation loop lines, the stress surface is likewise unsymmetric. However, Fig. 16 shows an interesting mirrorlike symmetry of the stress σ_{11} isosurface and the original geometry of the FR sources. This observation is only seen at high levels of stress, where there is nearly no overlap between the stress fields of various segments of the dislocation microstructure. In any event, going beyond the configurations presented here would introduce additional complexities, which are best utilized in computations of Peach-Kohler forces on dislocation segments.

FIG. 14. Shear stress distribution resulting from the interaction of a single FR source with the surface of a molybdenum single crystal.
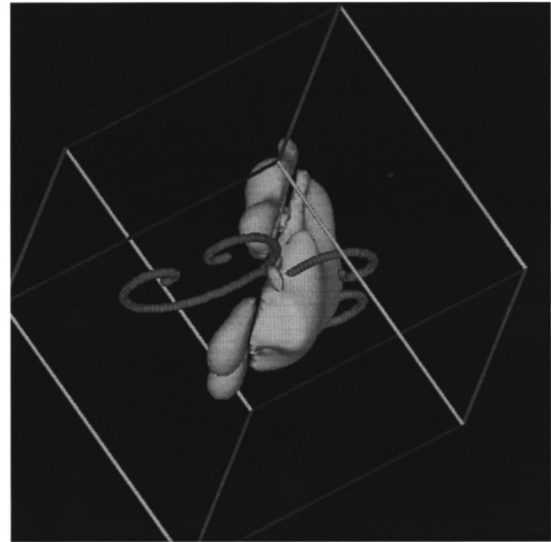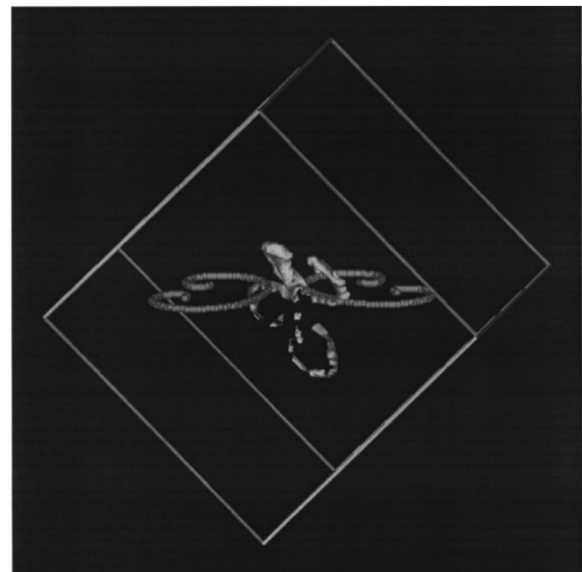

FIG. 16. Normal stress isosurface (-2000 MPa) σ_{11} for two interacting Frank-Read sources in molybdenum.

V. CONCLUSIONS

The fast-sum method, which is based on a combination of dislocation loop geometry parametrization and numerical quadrature integrations along parametrized curves, is shown to be computationally feasible and highly accurate. All calculations involve simple algebraic operations, which can be systematically carried out by straightforward computer programming. Although we used FORTRAN-90 to implement the results of calculations, even spreadsheets on personal computers can be effectively utilized. The method is as efficient as analytical solutions. The index structure associated with tensor notation simplifies computer programming of the equation. However, because analytical solutions are available only for a limited number of special cases, the present approach can be used for calculations involving complex loop geometries. The present method is primarily intended for applications in dislocation dynamics computer simulations, where the need for accuracy is critical in close-range dislocation encounters. Moreover, one may consider the present method as an extension of the FEM technique in continuum mechanics. A variety of parametrized elements can thus be chosen (in much the same way as in the FEM approach) to handle special dislocation deformation problems. The method may also be exploited in crack problems, where dislocation distributions can be used to represent complex crack surfaces.

To handle the effects of free crystal surfaces on the redistribution of the elastic field inside the crystal, and hence on computed Peach-Kohler forces, the superposition method of Cleveringa *et al.* is extended to 3D applications. While only 2D problems have been solved so far by their method, we show that 3D problems can also be successfully implemented. However, the simple problem shown here required almost 30 000 degrees of freedom and the utilization of 3D (27-node) brick elements. Other methods [e.g., the boundary integral method] may be more appropriate for 3D computer simulations, since the stress field should be updated very frequently during dislocation dynamics computer simulations.

APPENDIX A: RADIUS VECTOR AND SOLID ANGLE

As shown in Fig. 17, the solid angle differential $d\Omega$ is the ratio of the projected area element $d\mathbf{S}$ to the square of R. Thus,
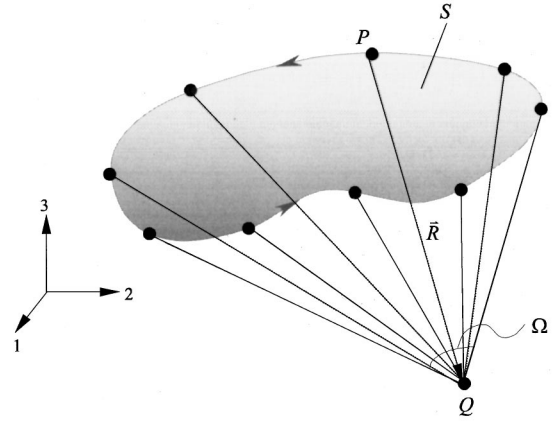

FIG. 17. Representation of the solid angle Ω at a field point (Q) away from the dislocation loop line containing the set of points (P).

$$\Omega = \int d\Omega = \int_S \frac{\mathbf{e} \cdot d\mathbf{S}}{R^2} = \int_S \frac{X_i dS_i}{R^3} = -\frac{1}{2}\int_S R_{,ppi}dS_i,$$

(A1)

where $\mathbf{e} = \mathbf{R}/R = \text{set}\{e_i\}$ is a unit vector along $\mathbf{R} = \text{set}\{X_i\}$, and $R_{,ppi} = -2X_i/R^3$. The solid angle can be computed as a line integral, by virtue of Stokes' theorem. A vector potential $\mathbf{A}(\mathbf{R})$ is introduced by deWit to satisfy the differential equation $\epsilon_{pik}A_{k,p}(\mathbf{R}) = X_i R^{-3}$. The solution is given by[42] $A_k(\mathbf{R}) = \epsilon_{ijk}X_i s_j/[R(R + \mathbf{R}\cdot\mathbf{s})]$, where $\mathbf{s}$ is an arbitrary unit vector. This results in a nonuniqueness of the displacement field, although it can be arbitrarily symmetrized.[41] The solid angle is then given as a line integral: $\Omega(\mathbf{R}) = \oint_C A_k(\mathbf{R})dl_k$. Taking the derivatives of Ω in Eq. (A1) and applying Eq. (3.6), we obtain

$$\Omega_{,j} = \frac{1}{2}\int_S (R_{,ppll}dS_j - R_{,pplj}dS_l) = \frac{1}{2}\oint_C \epsilon_{jkl}R_{,ppl}dl_k.$$

(A2)

Successive derivatives of the vector $\mathbf{R}$ are given by the following set of equations:

$$R_{,i} = \frac{X_i}{(X_q X_q)^{1/2}} = \frac{X_i}{R} = e_i,$$

(A3)

$$R_{,ij} = \frac{\delta_{ij}}{(X_q X_q)^{1/2}} - \frac{X_i X_j}{(X_q X_q)^{3/2}} = \frac{\delta_{ij}}{R} - \frac{X_i X_j}{R^3} = (\delta_{ij} - e_i e_j)/R,$$

(A4)

$$R_{,ijk} = -\frac{\delta_{jk}X_i + \delta_{ik}X_j + \delta_{ij}X_k}{(X_q X_q)^{3/2}} + \frac{3X_i X_j X_k}{(X_q X_q)^{5/2}}$$

(A5)

$$= -\frac{\delta_{jk}X_i + \delta_{ik}X_j + \delta_{ij}X_k}{R^3} + \frac{3X_i X_j X_k}{R^5}$$

$$= (3e_i e_j e_k - [\delta_{ij}e_k + \delta_{jk}e_i + \delta_{ki}e_j])/R^2.$$ (A6)

The third-rank tensor $R_{,ijk}$ has only ten nonvanishing terms, and these are given below for convenience:

$$R_{,111} = 3e_1(e_1^2 - 1)/R^2, \quad R_{,112} = e_2(3e_1^2 - 1)/R^2,$$

$$R_{,113} = e_3(3e_1^2 - 1)/R^2,$$

(A7)

$$R_{,221}=e_1(3e_2^2-1)/R^2, \quad R_{,222}=3e_2(e_2^2-1)/R^2, \qquad\qquad\qquad R_{,333}=3e_3(e_3^2-1)/R^2, \tag{A9}$$

$$R_{,223}=e_3(3e_2^2-1)/R^2, \tag{A8}$$

$$R_{,331}=e_1(3e_3^2-1)/R^2, \quad R_{,332}=3e_2(3e_3^2-1)/R^2, \qquad\qquad\qquad R_{,123}=3e_1e_2e_3/R^2. \tag{A10}$$

APPENDIX B: STRESS TENSOR COMPONENTS

For one loop, explicit fast-sum forms of the three-dimensional stress tensor components are given below. The inner sum is extended over the number of quadrature points assigned in the interval $-1 \le \hat{u} \le 1$. $Q_{\max}$ is typically 8–16 for accurate results, although cases with $Q_{\max}$ up to 300 have been tested. The outer sum is over the number of loop segments, which is typically in the range 10–30. For an arbitrary number of loops of defined parametric geometry, a third sum over the loop number must additionally be included:

$$
\begin{aligned}
\sigma_{11}=\frac{\mu}{8\pi}\sum_{\gamma=1}^{N_{\text{loop}}}\sum_{\beta=1}^{N_s}\sum_{\alpha=1}^{Q_{\max}} w_\alpha &\left\{\left[b_2\left(-2R_{,113}+\frac{2\nu}{1-\nu}(R_{,223}+R_{,333})\right)+b_3\left(2R_{,112}-\frac{2\nu}{1-\nu}(R_{,222}+R_{,332})\right)\right]\hat{x}_{1,u}\right.\\
&+\left[-b_1\frac{2}{1-\nu}(R_{,223}+R_{,333})+b_3\frac{2}{1-\nu}(R_{,221}+R_{,331})\right]\hat{x}_{2,u}\\
&\left.+\left[+b_1\frac{2}{1-\nu}(R_{,222}+R_{,332})-b_2\frac{2}{1-\nu}(R_{,221}+R_{,331})\right]\hat{x}_{3,u}\right\}_\alpha,
\end{aligned}\tag{B1}
$$

$$
\begin{aligned}
\sigma_{12}=\frac{\mu}{8\pi}\sum_{\gamma=1}^{N_{\text{loop}}}\sum_{\beta=1}^{N_s}\sum_{\alpha=1}^{Q_{\max}} w_\alpha &\left\{\left[b_1(R_{,113}+R_{,223}+R_{,333})-b_2\left(\frac{2}{1-\nu}R_{,123}\right)+b_3\left(\frac{1+\nu}{1-\nu}R_{,221}-R_{,111}-R_{,331}\right)\right]\hat{x}_{1,u}\right.\\
&+\left[b_1\left(\frac{2}{1-\nu}R_{,123}\right)-b_2(R_{,113}+R_{,223}+R_{,333})+b_3\left(-\frac{1+\nu}{1-\nu}R_{,112}+R_{,222}+R_{,332}\right)\right]\hat{x}_{2,u}\\
&\left.+\frac{2}{1-\nu}(-b_1R_{,221}+b_2R_{,112})\hat{x}_{3,u}\right\}_\alpha,
\end{aligned}\tag{B2}
$$

$$
\begin{aligned}
\sigma_{13}=\frac{\mu}{8\pi}\sum_{\gamma=1}^{N_{\text{loop}}}\sum_{\beta=1}^{N_s}\sum_{\alpha=1}^{Q_{\max}} w_\alpha &\left\{\left[-b_1(R_{,112}+R_{,222}+R_{,332})+b_2\left(R_{,111}+R_{,221}-\frac{1+\nu}{1-\nu}R_{,331}\right)+b_3\left(\frac{2}{1-\nu}R_{,123}\right)\right]\hat{x}_{1,u}\right.\\
&+\frac{2}{1-\nu}(b_1R_{,331}-b_3R_{,113})\hat{x}_{2,u}+\left[-b_1\left(\frac{2}{1-\nu}R_{,123}\right)-b_2\left(-\frac{1+\nu}{1-\nu}R_{,113}+R_{,223}+R_{,333}\right)\right.\\
&\left.\left.+b_3(R_{,112}+R_{,222}+R_{,332})\right]\hat{x}_{3,u}\right\}_\alpha,
\end{aligned}\tag{B3}
$$

$$
\begin{aligned}
\sigma_{22}=\frac{\mu}{8\pi}\sum_{\gamma=1}^{N_{\text{loop}}}\sum_{\beta=1}^{N_s}\sum_{\alpha=1}^{Q_{\max}} w_\alpha &\left\{\left[b_2\frac{2}{1-\nu}(R_{,113}+R_{,333})-b_3\frac{2}{1-\nu}(R_{,112}+R_{,332})\right]\hat{x}_{1,u}+\left[b_1\left(-\frac{2\nu}{1-\nu}(R_{,113}+R_{,333})+2R_{,223}\right)\right.\right.\\
&\left.\left.+b_3\left(\frac{2\nu}{1-\nu}(R_{,111}+R_{,331})-2R_{,221}\right)\right]\hat{x}_{2,u}+\left[b_1\frac{2}{1-\nu}(R_{,112}+R_{,332})-b_2\frac{2}{1-\nu}(R_{,111}+R_{,331})\right]\hat{x}_{3,u}\right\}_\alpha,
\end{aligned}\tag{B4}
$$

$$
\begin{aligned}
\sigma_{23}=\frac{\mu}{8\pi}\sum_{\gamma=1}^{N_{\text{loop}}}\sum_{\beta=1}^{N_s}\sum_{\alpha=1}^{Q_{\max}} w_\alpha &\left\{\left[-b_2\frac{2}{1-\nu}R_{,332}+b_3\frac{2}{1-\nu}R_{,223}\right]\hat{x}_{1,u}+\left[b_1\left(-R_{,112}-R_{,222}+\frac{1+\nu}{1-\nu}R_{,332}\right)\right.\right.\\
&\left.+b_2(R_{,111}+R_{,221}+R_{,331})-b_3\left(\frac{2}{1-\nu}R_{,123}\right)\right]\hat{x}_{2,u}+\left[b_1\left(R_{,113}+R_{,333}-\frac{1+\nu}{1-\nu}R_{,223}\right)+b_2\left(\frac{2}{1-\nu}R_{,123}\right)\right.\\
&\left.\left.-b_3(R_{,111}+R_{,221}+R_{,331})\right]\hat{x}_{3,u}\right\}_\alpha,
\end{aligned}\tag{B5}
$$

$$\sigma_{33} = \frac{\mu}{8\pi} \sum_{\gamma=1}^{N_{\text{loop}}} \sum_{\beta=1}^{N_s} \sum_{\alpha=1}^{Q_{\text{max}}} w_\alpha \left\{ \left[+b_2 \frac{2}{1-\nu}(R_{,113}+R_{,223}) - b_3 \frac{2}{1-\nu}(R_{,112}+R_{,222}) \right] \hat{x}_{1,u} + \left[-b_1 \frac{2}{1-\nu}(R_{,113}+R_{,223}) \right.\right.$$

$$\left.\left. + b_3 \frac{2}{1-\nu}(R_{,111}+R_{,221}) \right] \hat{x}_{2,u} + \left[+b_1 \left(\frac{2\nu}{1-\nu}(R_{,112}+R_{,222}) - 2R_{,332} \right) + b_2 \left(-\frac{2\nu}{1-\nu}(R_{,111}+R_{,221}) + 2R_{,331} \right) \right] \hat{x}_{3,u} \right\}_\alpha .$$

(B6)

[1] F. R. N. Nabarro, *Theory of Crystal Dislocations* (Clarendon, Oxford, 1967).

[2] J. P. Hirth and J. Lothe, *Theory of Dislocations*, 2nd ed. (McGraw-Hill, New York, 1982).

[3] R. Bullough and R.C. Newman, Philos. Mag. **5**, 921 (1960).

[4] E. Kröner, *Kontinuumstheorie der Versetzungen und Eigenspannungen* (Springer, Berlin, 1958).

[5] F. Kroupa, Czech. J. Phys., Sect. B **10**, 284 (1960).

[6] F. Kroupa, in *Theory of Crystal Defects*, edited by B. Gruber (Academia Publishing House, Prague, 1966), p. 275.

[7] R. deWit, Solid State Phys. **10**, 269 (1960).

[8] R.J. Amodeo and N.M. Ghoniem, Res. Mech. **23**, 137 (1988).

[9] H. Mughrabi, Mater. Sci. Eng. **85**, 15 (1987).

[10] H. Mughrabi, Acta Metall. **31**, 1367 (1983).

[11] A.J.E. Forman, Philos. Mag. **17**, 353 (1968).

[12] J. Lepinoux and L.P. Kubin, Scr. Metall. **21**, 833 (1987).

[13] N.M. Ghoniem and R. Amodeo, Solid State Phenom. **3&4**, 377 (1988).

[14] R.J. Amodeo and N.M. Ghoniem, Int. J. Eng. Sci. **26**, 653 (1988).

[15] A.N. Guluoglu, D.J. Srolovitz, R. LeSar, and R.S. Lomdahl, Scr. Metall. **23**, 1347 (1989).

[16] N. M. Ghoniem and R. J. Amodeo, in *Patterns, Defects and Material Instabilities*, edited by D. Walgreaf and N. M. Ghoniem (Kluwer Academic, Dordrecht, 1990), p. 303.

[17] R.J. Amodeo and N.M. Ghoniem, Phys. Rev. B **41**, 6958 (1990).

[18] R.J. Amodeo and N.M. Ghoniem, Phys. Rev. B **41**, 6968 (1990).

[19] R. J. Amodeo, and N. M. Ghoniem, in *Modeling of Deformation of Crystalline Solids*, edited by T. Lowe, T. Rollett, P. Follansbee, and G. Daehn (TMS Press, Warrendale, PA, 1991), p. 125.

[20] N. M. Ghoniem, in *Non-Linear Phenomena in Material Science II*, edited by L. Kubin and G. Martin (Kluwer Academic, Dordrecht, 1992).

[21] I. Groma and G.S. Pawley, Philos. Mag. A **67**, 1459 (1993).

[22] V.A. Lubarda, I.A. Blume, and A. Needleman, Acta Metall. Mater. **41**, 625 (1993).

[23] A. Elazab and N.M. Ghoniem, Int. J. Fract. **61**, 17 (1993).

[24] H.Y. Wang and R. Lesar, Philos. Mag. A **71**, 149 (1995).

[25] L.P. Kubin, G. Canova, M. Condat, B. DeVincre, V. Pontikis, and Y. Brechet, Solid State Phenom. **23-24**, 445 (1992).

[26] B. DeVincre and M. Condat, Acta Metall. Mater. **40**, 2629 (1992).

[27] B. DeVincre, V. Pontikis, Y. Brechet, G. Canova, M. Condat, and L. P. Kubin, in *Microscopic Simulations of Complex Hydrodynamic Phenomena*, edited by M. Mareschal and B. L. Lolian (Plenum Press, New York, 1992), pp. 413–423.

[28] G. Canova, Y. Brechet, and L. P. Kubin, in *Modeling of Plastic Deformation and its Engineering Applications*, edited by S. I. Anderson *et al.* (RISØ National Laboratory, Roskilde, Denmark, 1992).

[29] L.P. Kubin and G. Canova, Scr. Metall. **27**, 957 (1992).

[30] L.P. Kubin, Phys. Status Solidi A **135**, 433 (1993).

[31] G. Canova, Y. Brechet, L. P. Kubin, B. DeVincre, V. Pontikis, and M. Condat, in *Microstructures and Physical Properties*, edited by J. Rabiet (CH-Transtech, Geneva, 1993).

[32] B. DeVincre and L.P. Kubin, Modell. Simul. Mater. Sci. Eng. **2**, 559 (1994).

[33] J.P. Hirth, M. Rhee, and H. Zbib, J. Comput.-Aided Mater. Des. **3**, 164 (1996).

[34] H.M. Zbib, M. Rhee, and J.P. Hirth, Int. J. Mech. Sci. **40**, 113 (1998).

[35] M. Rhee, H.M. Zbib, J.P. Hirth, H. Huang, and T. de la Rubia, Modell. Simul. Mater. Sci. Eng. **6**, 467 (1998).

[36] K.W. Schwarz and J. Tersoff, Appl. Phys. Lett. **69**, 1220 (1996).

[37] K.W. Schwarz, Phys. Rev. Lett. **78**, 4785 (1997).

[38] K.W. Schwarz and Le Goues, Phys. Rev. Lett. **79**, 1877 (1997).

[39] L.M. Brown, Philos. Mag. **15**, 363 (1967).

[40] T. Mura, *Micromechanics of Defects in Solids* (Martinus Nijhoff, The Hague, The Netherlands, 1982).

[41] M.O. Peach and J.S. Koehler, Phys. Rev. **80**, 436 (1950).

[42] R. deWit, in *Dislocation Modeling of Physical Systems*, edited by M. F. Ashby, R. Bullough, C. S. Hartley, and J. P. Hirth (Pergamon Press, Oxford, 1980), p. 305.

[43] N.M. Ghoniem, J. Eng. Mater. Technol. **121**, 136 (1999).

[44] N.M. Ghoniem and M. Bacaloni (unpublished).

[45] S. Amelinckx, *The Direct Observation of Dislocations* (Academic Press, New York, 1964).

[46] S.D. Gavazza and D.M. Barnett, J. Mech. Phys. Solids **24**, 171 (1976).

[47] E. Kröner, Ergrb. Angew. Math. **5**, 1 (1958).

[48] J.M. Burgers, Proc. K. Ned. Akad. Wet. **42**, 293 (1939).

[49] H. Cleveringa, E. Van der Giessen, and A. Needleman, J. Phys. I **8**, 83 (1998).